Journal of Colloid and Interface Science 699 (2025) 138251

Contents lists available at ScienceDirect

Journal of Colloid And Interface Science

journal homepage: www.elsevier.com/locate/jcis

Bismuth oxide–loaded indium–organic framework catalysts for efficient electrochemical CO_2 reduction

Fajun Li [a,b,c,*], Yuqi Ma [a,b], Lei Zhao [b], Lu Han [a], Xuancheng Gong [a], Yulu Zhang [a], Pengfei Lu [a], Guizhi Wang [a], Zhisheng Shi [b,d,*], Zhong Jin [a,c,**]

[a] School of Chemistry and Chemical Engineering, Anhui Key Laboratory of Spin Electron and Nanomaterials, Suzhou University, Suzhou 234000, China
[b] School of Chemical and Environmental Engineering, Anhui Laboratory of Clean Energy Materials and Chemistry for Sustainable Conversion of Natural Resources, Anhui Polytechnic University, Wuhu 241000, China
[c] School of Chemistry and Chemical Engineering, Nanjing University, Nanjing 210023, China
[d] Anhui Conch Group Co., Ltd, Jinghu District, Wuhu 241100, China

GRAPHICAL ABSTRACT

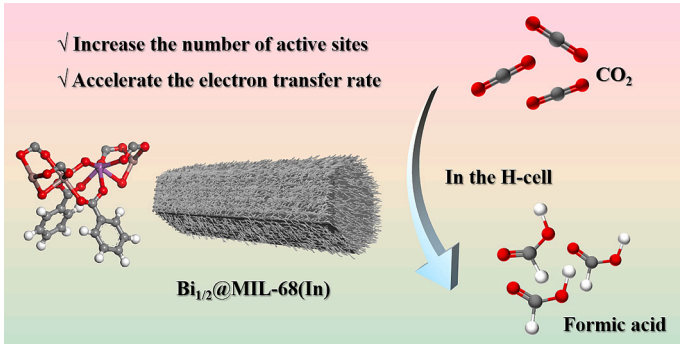

ARTICLE INFO

Keywords:
MIL-68(In)
Bismuth doping
Formic acid
Electrocatalytic CO_2 reduction
Catalytic activity

ABSTRACT

This study investigated electrocatalytic CO_2 reduction using bismuth oxide–loaded indium–organic framework catalysts (MIL-68(In)). Bismuth incorporation increased the density of reactive sites, reduced the energy barrier for intermediate formation, and significantly enhanced formic acid production. In an H-type cell, the $Bi_{1/2}$@MIL-68(In) catalyst achieved a Faradaic efficiency of 96.9 % for formic acid production at −1.7 V (vs. Ag/AgCl). Experimental results further confirmed that Bi^{3+} doping enhanced catalyst conductivity and accelerated electron transfer. The integration of Bi_2O_3 into the MIL-68(In) framework enriched the surface with reactive centers, thereby facilitating CO_2 adsorption and activation. Theoretical calculations revealed that $Bi_{1/2}$@MIL-68(In) stabilized the HCOO* intermediate, thereby reducing the free energy barrier for formic acid formation. This study highlights the potential of metal-organic frameworks (MOFs) as scaffolds for incorporating secondary

* Corresponding authors at: School of Chemistry and Chemical Engineering, Anhui Key Laboratory of Spin Electron and Nanomaterials, Suzhou University, Suzhou 234000, China; School of Chemical and Environmental Engineering, Anhui Laboratory of Clean Energy Materials and Chemistry for Sustainable Conversion of Natural Resources, Anhui Polytechnic University, Wuhu 241000, China.
** Corresponding author at: School of Chemistry and Chemical Engineering, Nanjing University, Nanjing 210023, China.
E-mail addresses: lifajuncl2012@163.com (F. Li), shizhisheng@ahpu.edu.cn (Z. Shi), zhongjin@nju.edu.cn (Z. Jin).

https://doi.org/10.1016/j.jcis.2025.138251
Received 5 March 2025; Received in revised form 17 June 2025; Accepted 19 June 2025
Available online 20 June 2025

metals to enhance catalytic performance. The findings provide valuable guidance for the rational design of highly efficient CO_2 reduction catalysts.

1. Introduction

Since the Industrial Revolution, the amount of carbon dioxide produced globally has consistently increased each year due to industrial production [1,2]. Excessive carbon dioxide emissions have sharply increased the frequency of natural disasters and hindered sustainable human development [3]. The scientific community has determined that the transformation of carbon dioxide into valuable chemicals and fuels can enhance the carbon cycle [4,5]. One such example is the electrocatalytic CO_2 reduction reaction (ECO_2RR), which shows exceptional environmental compatibility [6–9]. Nevertheless, the stable thermodynamic characteristics of carbon dioxide molecules make them difficult to activate [10]. Hence, activating chemically inert carbon dioxide molecules and facilitating their chemical conversion under mild conditions constitute a major research challenge [11].

Research has suggested that using diverse catalysts and precisely controlling reaction conditions allows carbon dioxide to be converted into a wide variety of carbon-based products. Formic acid is one such electrolysis-derived product that shows remarkable commercial and industrial significance [12,13]. Beyond its use for hydrogen storage, this compound has also found applications in pharmaceuticals, rubber, and chemicals [14–16]. Among different catalyst materials, indium-based catalysts have shown a high selectivity towards formic acid and an outstanding Faradaic efficiency (FE) [17–19]. However, these catalysts exhibit limited reactivity during CO_2 reduction. Research has revealed that the electrochemical carbon dioxide reduction reaction (ECO_2RR) to formic acid by indium-based catalysts can be enhanced by several methods. Examples include modulating indium's electronic structure and crystalline surface exposure, constructing composite catalysts, and surface modification and doping. Li et al. transformed two-dimensional indium coordination polymers into elemental indium nanosheets to yield electrocatalysts with exceptional performance. They further showed that increasing the number of exposed catalyst active sites and increasing the charge transfer rate promoted the formation of intermediates during the reduction process, thereby markedly enhancing the catalyst's activity [20]. Similarly, Wulan et al. optimized the structure of their catalysts and fine-tuned their surface properties by modulating interfacial oxygen on layered indium oxide nanosheets [21]. Cheng et al., on the other hand, investigated the influence of oxygen vacancy concentration in indium oxide on the catalytic performance of ECO_2RR by using a rational design approach to introduce oxygen vacancies within indium oxide nanorods [22].

Metal-organic frameworks (MOFs) are composed of a central metal atom that forms coordination bonds with organic ligands [23–25]. MOFs with a rich diversity of pore sizes and structures can be fabricated by modifying the metal nodes and organic ligands. Due to their unique architectures, high specific surface area, and tunable pore dimensions, MOFs have increasingly captured the focus of researchers working in catalysis [26,27]. MIL-68(In) is a MOF characterized by a hexagonal prismatic rod structure, whose tubular conformation gives it a high specific surface area and tendency to expedite charge-transfer processes. The existence of open metal sites within MOFs creates opportunities for the attachment of additional functional groups to enhance its catalytic properties [28,29]. Wang et al. fabricated MIL-68(In)-NH_2 electrocatalysts by assembling amino functional groups onto MIL-68(In) [30]. Their research showed that the integration of amino groups promoted more effective CO_2 activation and enhanced the formic acid generation capacity of the catalyst. Carbon-coated metal oxides can be synthesized via high-temperature annealing of MOF precursors. The incorporation of carbon protects metal oxides against reduction and expedites charge transfer, further optimizing charge movement during a reaction [31]. Pan et al. prepared indium oxide nanoparticles by subjecting MIL-68(In) to high-temperature annealing and then attached them to carbon nanotubes [32]. The resultant catalyst exhibited a high current density within the gas diffusion electrode. Similarly, Wang et al. adopted the carbon confinement strategy to encase the annealed indium oxide nanorods in carbon [33]. It was found that the carbon layer played a protective role, augmenting the electrical conductivity of the catalyst and, consequently, improving its catalytic performance.

Herein, Bi_x@MIL-68(In) (x = 1/2, 1/4, 1/6, 1/8) catalysts were synthesized by incorporating Bi^{3+} into MIL-68(In). Of these, $Bi_{1/2}$@MIL-68(In) exhibited outstanding electrocatalytic performance for CO_2 reduction compared with MIL-68(In), and it achieved a FE of 96.9 % for formic acid generation at −1.7 V (vs. Ag/AgCl). Bi^{3+} doping improved conductivity and electron transfer, while Bi_2O_3 loading increased active sites, which in turn enhanced the CO_2 adsorption and formic acid yield. Using MOFs as a scaffold for metal loading boosted the catalytic activity, thus providing valuable insights for the rational design of CO_2 reduction catalysts.

2. Experimental section

2.1. Chemicals and reagents

Indium nitrate hydrate ($In(NO_3)_3{\cdot}H_2O$, 99.99 %), Bismuth nitrate pentahydrate ($Bi(NO_3)_3{\cdot}5H_2O$, 99.0 %) were all available from Aladdin. p-Phthalic acid (H_2BDC, 99 %), *N*,*N*-Dimethylformamide (DMF, 99.5 %) and ethanol (99.9 %) were all available from Maclin. All of the reagents were used as received without further purification. High-purity argon (Ar, 99.999 %) and carbon dioxide (CO_2, 99.999 %) were purchased from Lingbi Yuyang Gas Co.

2.2. Preparation of the samples

(1) Preparation of MIL-68(In)

Firstly, 0.5988 g of $In(NO_3)_3{\cdot}H_2O$ and 0.2151 g of H_2BDC were dissolved in a 20 mL of DMF solution. Subsequently, the resultant mixture was stirred continuously for 30 min under room temperature conditions. Afterward, it was carefully poured into a 50 mL Teflon liner that was fitted inside a stainless-steel autoclave. The entire reaction kettle was then transferred to an oven pre-set at 100 °C and left to react for 48 h. Upon completion of the reaction, the system was allowed to cool down naturally. Once cooled, the white precipitate that had formed was separated by centrifugation and washed three times with anhydrous ethanol to remove impurities. Finally, the purified sample was then placed in a vacuum drying oven set at 60 °C for a duration of 12 h to ensure complete drying.

(2) Preparation of Bi_x@MIL-68(In) (x = 1/2, 1/4, 1/6, 1/8)

Take the synthesis of $Bi_{1/2}$@MIL68(In) as an illustration. Initially, 0.5986 g of $In(NO_3)_3{\cdot}H_2O$ and 0.4821 g of $Bi(NO_3)_3{\cdot}5H_2O$ were dissolved in a 10 mL volume of DMF solution and stirred vigorously for 30 min. Meanwhile, 0.2149 g of H_2BDC was dissolved in another 10 mL portion of DMF solution and stirred for 30 min as well. Subsequently, the two aforementioned mixtures were combined and further stirred for an additional 30 min to ensure thorough mixing. Thereafter, the combined mixture was poured into a 50 mL Teflon-lined stainless-steel autoclave. The reaction autoclave was then transferred to an oven maintained at 100 °C and allowed to react for 48 h. Upon the completion of the reaction, the system was left to cool down naturally. Once cooled, the

white precipitate that had formed was separated by centrifugation and washed three times with anhydrous ethanol to remove impurities. Subsequently, the purified sample was placed in a vacuum drying oven set at 60 °C for 12 h to achieve proper drying. Finally, the substantial amount of the white product was designated as $Bi_{1/2}$@MIL-68(In).

The remaining ratios of Bi_x@MIL-68(In) were synthesized using a similar method. The only difference lay in the amounts of bismuth metal ions added: for $Bi_{1/4}$@MIL-68(In), 0.2411 g of $Bi(NO_3)_3{\cdot}5H_2O$ was used; for $Bi_{1/6}$@MIL-68(In), 0.1607 g of $Bi(NO_3)_3{\cdot}5H_2O$ was used; and for $Bi_{1/8}$@MIL-68(In), 0.1205 g of $Bi(NO_3)_3{\cdot}5H_2O$ was used.

Preparation of $BiInO_x$: 0.15 g sample of $Bi_{1/2}$@MIL-68(In) was placed in a crucible and then heated in a muffle furnace. The temperature was raised at a rate of 5 °C/min until it reached 450 °C and was maintained at this temperature for 4 h. After the heating process, a yellow powder, namely $BiInO_x$, was obtained.

2.3. Material characterizations

The surface morphology information of the samples were characterized by scanning electron microscope (SEM, Gemini SEM 300, Zeiss) and transmission electron microscope (TEM, JEM-F200, Jeol). The phase structures of the samples were determined by powder Xray diffraction (XRD, D8 Focus, Bruker). The chemical bonding and molecular structure of the catalysts were tested using infrared spectroscopy (FTIR, IRPrestige-21, Shimadzu). The elemental composition of the catalysts were determined using an X-ray photoelectron spectrometer (XPS, K-Alpha, Thermo Fisher Scientific). The elemental content and distribution of the materials were further analyzed using a scanning electron microscope-energy dispersive X-ray spectroscopy (EDS, S-4800, Hitachi). The products were determined by gas chromatography (GC, GC9790II, Zhejiang Fuli Analytical Instruments Corp) and Ion chromatography (IC, CIC-D120, Qingdao Shenghan Chromatography Technology Co.).

2.4. Electrochemical measurements

Preparation of working electrode: To fabricate the working electrode, 5 mg of the catalyst was first weighed out and mixed with 1 mL of deionized water. The mixture was then subjected to sonication for a period of 30 min to achieve thorough dispersion. Subsequently, 6 μL of the resulting slurry was carefully pipetted and uniformly drop-coated onto the surface of a glassy carbon electrode with a diameter of 5 mm. After the drop-coating process, the electrode was left to dry at room temperature. Following this, 6 μL of a 10 wt% Nafion solution was taken and gently dropped onto the surface of the already-coated glassy carbon electrode. Finally, the electrode was allowed to dry naturally.

In this experimental setup, a glassy carbon electrode served was employed as the working electrode, while the Ag/AgCl electrode and Pt sheet served as the reference electrode and counter electrode, respectively. The electrolyte employed was a 0.1 M $KHCO_3$ solution with an initial pH value of 8.41. Carbon dioxide gas was bubbled into the solution until it reached saturation at room temperature and atmospheric pressure, resulting in a pH decrease to 6.73. Subsequently, when the solution was saturated with an adequate amount of argon gas, the pH rose to 8.68. Cyclic voltammetry (CV) and linear sweep voltammetry (LSV) curves were recorded using a CHI760E electrochemical workstation (manufactured by ChenHua Instruments, Shanghai). These measurements were carried out in both CO_2-saturated and Ar-saturated 0.1 M $KHCO_3$ solutions, at a scan rate of 10 mV s^{-1} in either the CO_2 or Ar atmosphere, sweeping the potential from 0 V to −1.8 V. The potentials can be converted to the Reversible Hydrogen Electrode (RHE) scale by applying the following equation: $E_{(vs\ RHE)} = E_{(vs\ Ag/AgCl)} + 0.197\ V + 0.0591 \times pH$. CV was also employed to assess the electrochemical surface area (ECSA) of the electrode and to estimate the capacitance of the double layer present on the surface of the material. A specific non-Faradaic potential region was chosen as the potential interval for this test, and scanning rates of 20, 40, 60, 80, and 100 mV s^{-1} were employed. The ECSA was calculated using the formula: $ECSA = R_f * S$, where S denotes the active surface area of the electrode. The roughness factor (R_f) was derived from the formula, $R_f = C_{dl}/C_s$. To illustrate the capacitance of the double layer, the variable Δj, defined as $\Delta j = j_a - j_c$ (where j_a and j_c represent the current densities of the anode and cathode, respectively), was plotted against the scan rate. The value of Δj at 0.12 V served as the vertical coordinate, while the scan rate was represented on the horizontal axis. Electrochemical impedance spectroscopy (EIS) measurements were conducted over a frequency range from 0.01 Hz to 100 kHz. The electrolyte solution used was a 0.1 M $KHCO_3$ solution, and the measurements were taken at −2 V.

Constant potential polarization: Under room temperature and atmospheric pressure conditions, carbon dioxide was introduced into a 0.1 M $KHCO_3$ solution for a minimum duration of 30 min to ensure saturation of the electrolyte with CO_2. Subsequently, the electrolyte was subjected to polarization at the designated potential for 30 min.

Product analysis was carried out using GC and IC. After completing the electrolysis process, the electrolyte was collected and the yield of the liquid product was quantified through IC. Simultaneously, the gas-phase product was collected in a gas collection bag, and its yield was quantified and analyzed through GC. The formula for calculating the FE of both gas-phase and liquid-phase products are as follows:

$$FE = \frac{nzF}{Q} \times 100\%$$

(where n is the molar amount of product, z is the number of electrons transferred during the reduction, F is the Faradaic constant and Q is the charge during the reaction.)

2.5. Calculation specification

Density functional theory (DFT) calculations were implemented using the Dmol^3 package. The pristine MIL-68(In) framework was derived from its crystallographic data, and the Bi-doped MIL-68(In) structure was generated by substituting a single indium (In) atom with bismuth (Bi). Subsequent geometry optimization and energy computations were performed within the DFT framework. The exchange-correlation interactions were treated with the generalized gradient approximation (GGA) using the Becke-Lee-Yang-Parr (BLYP) functional. Valence electron wavefunctions were expanded via a double-numerical basis set incorporating polarization functions (DNP), while core electrons were addressed through the DFT semi-core pseudopotential (DSPP). Convergence criteria for structural optimization were set at 0.04 Ha/Å for atomic forces and 2×10^{-5} Ha for total energy tolerance. Molecular configurations of H_2, CO_2, COOH, and HCOOH, along with their adsorption complexes on $Bi_{1/2}$@MIL-68(In), were systematically optimized using identical computational protocols. The binding energy (E_b) was determined through: $E_b = E_{complex} - (E_{Bi1/2@MIL\text{-}68(In)} + E_{adsorbate})$ where $E_{complex}$, $E_{Bi1/2@MIL\text{-}68(In)}$, and $E_{adsorbate}$ represent the total energies of the adsorbed system, pristine framework, and isolated adsorbate (H_2/CO_2/COOH/HCOOH), respectively.

3. Results and discussion

3.1. Synthesis and structural characterization

The synthesis of Bi_x@MIL-68(In) is illustrated in Fig. 1, with the only variation being the amounts of bismuth metal ions incorporated.

The SEM image in Fig. 2a provides definitive evidence of the micrometer-scale rod-like architecture of MIL-68(In). The surfaces of these rods were smooth, and their termini were sealed, with lengths ranging from 10 μm to 30 μm and widths from 300 nm to 500 nm. Fig. 2b illustrates that $Bi_{1/2}$@MIL-68(In) maintained a rod-like morphology, but a greater number of filamentary clusters emerged on its surface, along

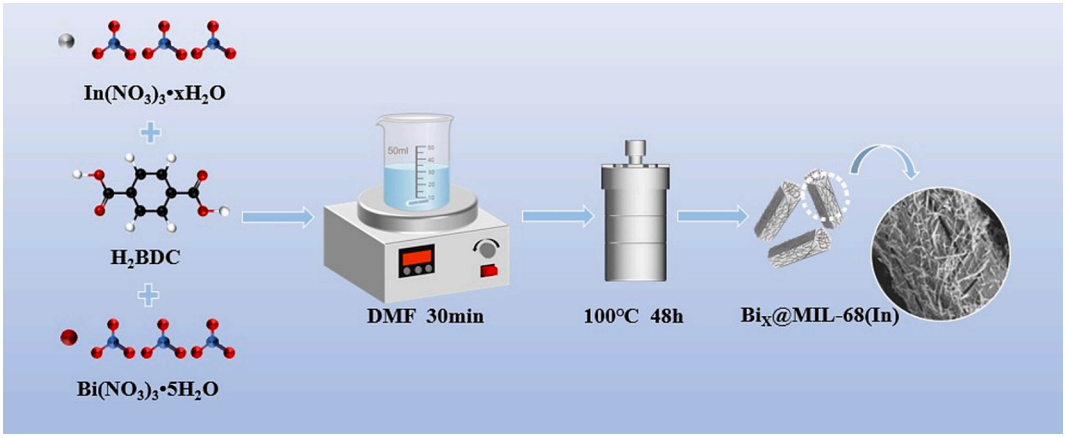

Fig. 1. Schematic representation of the preparation of Bi_x@MIL-68(In).

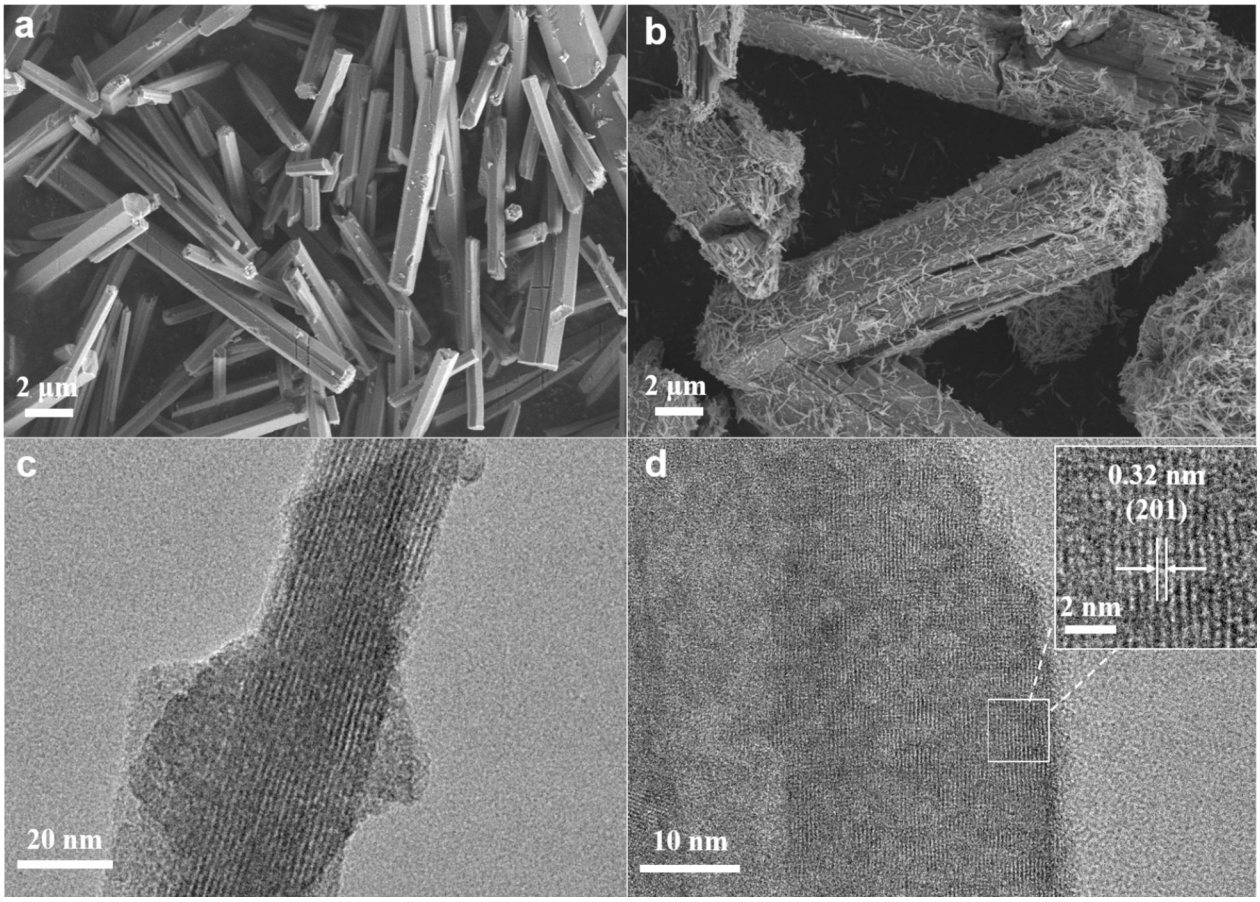

Fig. 2. SEM images of (a) MIL-68(In) and (b) $Bi_{1/2}$@MIL-68(In); (c, d) TEM images of $Bi_{1/2}$@MIL-68(In).

with multiple fissures within the rods. These changes increased both the specific surface area and the quantity of active sites. The clustering became increasingly pronounced upon progressively increasing the bismuth content, while the tubular structure facilitated more efficient charge transfer, thereby enhancing the catalytic efficacy of the catalyst.

To investigate the effects of annealing on the structural properties of $Bi_{1/2}$@MIL-68(In), an annealing procedure was conducted. $Bi_{1/2}$@MIL-68(In) was heated at a rate of 5 °C/min until it reached 450 °C, followed by a hold at this temperature for 4 h. **Fig. S1** displays the SEM image of $BiInO_x$, revealing the formation of new microscopic pores into its rod structure after annealing. Nanoparticles attached to the MIL-68(In) framework were visualized using TEM (Fig. 2c, d), in which the lattice fringe corresponded to the (201) crystallographic plane of Bi_2O_3, providing additional evidence for the successful incorporation of Bi onto MIL-68(In). The EDS element map of $Bi_{1/2}$@MIL-68(In) confirmed the presence of Bi, In, C, and O, with corresponding atomic ratios of 2.77: 4.79: 35.13: 57.31. These elements were uniformly distributed throughout the Bi_x@MIL-68(In) sample, confirming the successful introduction of Bi into MIL-68(In). The EDS element maps provided further evidence that the doping of bismuth at different molar ratios generally followed a regular pattern, but there were inevitable losses during the doping procedure, as illustrated in **Fig. S2**.

The XRD analysis revealed that the characteristic peaks of the synthesized MIL-68(In) strongly correlated with those reported in the literature, as illustrated in Fig. 3a. Prominent peaks were observed at 8.12°, 9.38°, 14.08°, 16.28°, 16.94°, 18.82°, 26.44°, 29.72°, and 31.22° [34], confirming the successful fabrication of MIL-68(In). The XRD patterns of bismuth-loaded MIL-68(In) in Fig. 3a show no significant changes in the diffraction peaks, indicating that the incorporation of bismuth did not alter the crystal structure of MIL-68(In) or affect the catalyst framework. The crystal structure of $Bi_{1/2}$@MIL-68(In) after annealing in a muffle furnace was characterized by XRD, as illustrated in **Fig. S3**, which showed that annealing converted indium in $Bi_{1/2}$@MIL-68(In) to In_2O_3. The resulting diffraction peaks observed at 21.5°, 30.6°, 35.5°, and 51° corresponded to the (221), (222), (400), and (440) crystallographic planes of cubic In_2O_3 (PDF NO.06–0416), respectively. The diffraction peaks at 27.9°, 32.7°, and 46.2° corresponded to the (201), (220), and (222) crystal planes of Bi_2O_3 (PDF NO.42–0196). The FTIR spectra in Fig. 3b demonstrate that both MIL-68(In) and Bi_x@MIL-68(In) displayed comparable peaks, and the absorption peak at 1661 cm^{-1} was ascribed to the C═O bonds of residual DMF [35].

The surface characteristics of $Bi_{1/2}$@MIL-68(In), including their valence compositions and variations, were further analyzed using XPS. As depicted in Fig. 3c, $Bi_{1/2}$@MIL-68(In) was primarily composed of C, O, In, and Bi elements. The high-resolution C 1 s spectrum of $Bi_{1/2}$@MIL-68(In) (Fig. 3d) contained three peaks at 284.8 eV, 285.7 eV, and 288.5 eV, corresponding to C═C, C—O, and C═O bonds, respectively [36]. Fig. 3e presents the high-resolution spectra of Bi 4f for $Bi_{1/2}$@MIL-68 (In). The spectra were deconvoluted into two characteristic peaks at 159.1 eV and 164.4 eV, corresponding to Bi $4f_{7/2}$ and Bi $4f_{5/2}$, respectively. This suggested that the oxidation state of Bi was +3, implying that Bi atoms were integrated into the MOFs skeleton as an oxide [37]. The high-resolution spectrum of In 3d for $Bi_{1/2}$@MIL-68(In) (Fig. 3f) reveals that the peaks at binding energies of 445.1 eV and 452.7 eV corresponded to In $3d_{5/2}$ and In $3d_{3/2}$ orbitals, respectively. This indicated that In atoms in the material existed as In^{3+} [38]. The Bi_2O_3 nanowires loaded onto the In-MOFs skeleton enhanced the stability of reaction intermediates, thus facilitating the reduction of CO_2 to formic acid. A comparison of XPS patterns of $BiInO_x$ and $Bi_{1/2}$@MIL-68(In) revealed a slight negative shift (**Fig. S4**), which demonstrated an increased electron density around In atoms after annealing. Such alterations in the electronic environment facilitated the stabilization of intermediates, thereby enhancing the CO_2 reduction process [39].

3.2. Electrochemical performance

The electrocatalytic activities of MIL-68(In) and Bi_x@MIL-68(In) for ECO_2RR were investigated by LSV, as depicted in Fig. 4a. The electrode functionalized with MIL-68(In) exhibited a slightly higher geometric current density in CO_2-saturated electrolyte than in an Ar-saturated electrolyte, suggesting that MIL-68(In) showed catalytic activity for ECO_2RR. The current density measured under an Ar atmosphere was ascribed to the hydrogen evolution reaction (HER), while the significant increase in current density under a CO_2 atmosphere was associated with the consumption of carbon dioxide. Additionally, the $Bi_{1/2}$@MIL-68(In) sample exhibited a better onset potential under a CO_2 atmosphere than under an Ar atmosphere. These findings strongly indicated that ECO_2RR was more likely to occur than HER on the surface of $Bi_{1/2}$@MIL-68(In). Fig. 4a clearly demonstrates that as the Bi loading increased, both the onset potential and current density under a CO_2 atmosphere rose, indicating improved carbon dioxide reduction. The total geometric current density of $Bi_{1/2}$@MIL-68(In) began to rise at −1.5 V (vs. Ag/AgCl), ultimately reaching −5.2 mA cm^{-2} at −1.8 V (vs. Ag/AgCl). In comparison, the other four samples possessed a more negative onset reduction potential and a lower current density. This demonstrated that the incorporation of Bi significantly enhanced the ECO_2RR capacity of MIL-68(In) materials. In addition, $BiInO_x$ exhibited favorable catalytic properties for ECO_2RR through experimental investigations (**Fig. S5a, S6**), and the CV curves further confirmed that Bi loading promoted carbon dioxide reduction (**Fig. S5b, S5c**).

A comprehensive exploration was undertaken to determine the factors underlying the remarkable catalytic performance of the Bi-doped MIL-68(In) catalysts. Initially, double-layer capacitors of MIL-68(In), $Bi_{1/8}$@MIL-68(In), $Bi_{1/6}$@MIL-68(In), $Bi_{1/4}$@MIL-68(In), and $Bi_{1/2}$@MIL-68(In) were examined to estimate ECSA. A higher ECSA value for a catalyst indicates a larger quantity of catalytically active sites, and

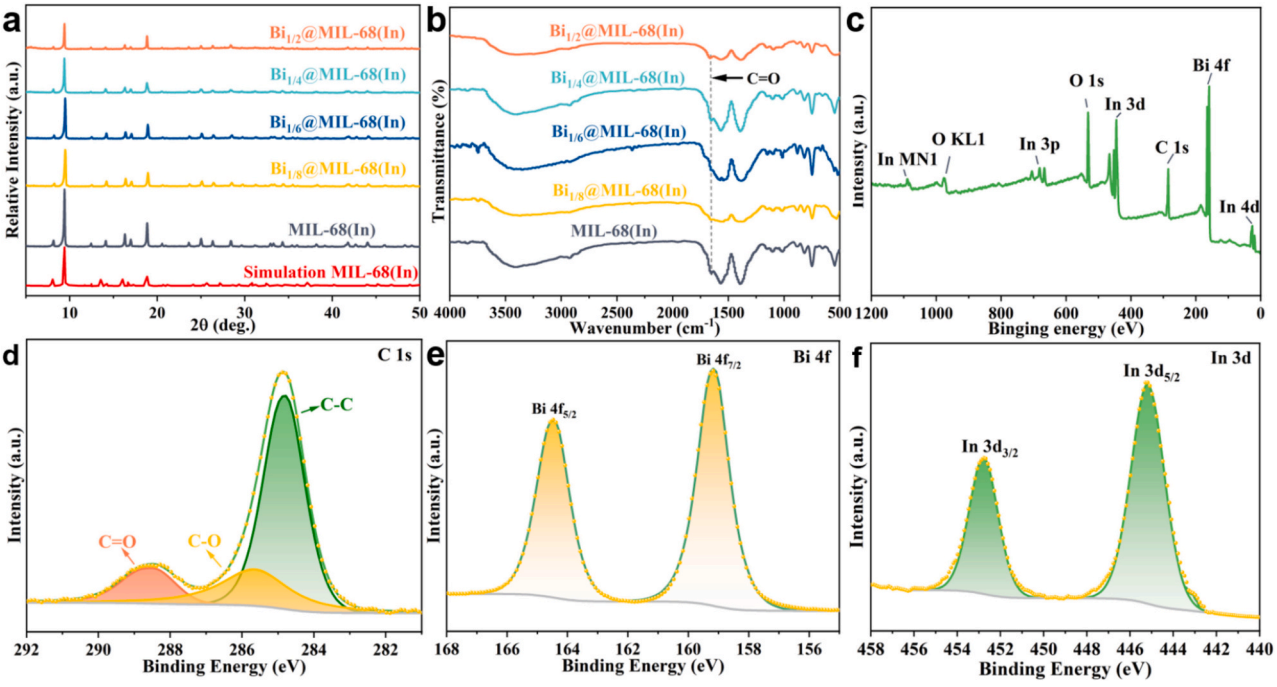

Fig. 3. (a) XRD patterns and (b) FTIR patterns of MIL-68(In) and Bi_x@MIL-68(In); (c) XPS full spectra of $Bi_{1/2}$@MIL-68(In); and high-resolution XPS spectra ((d) C 1 s, (e) Bi 4f, (f) In 3d).

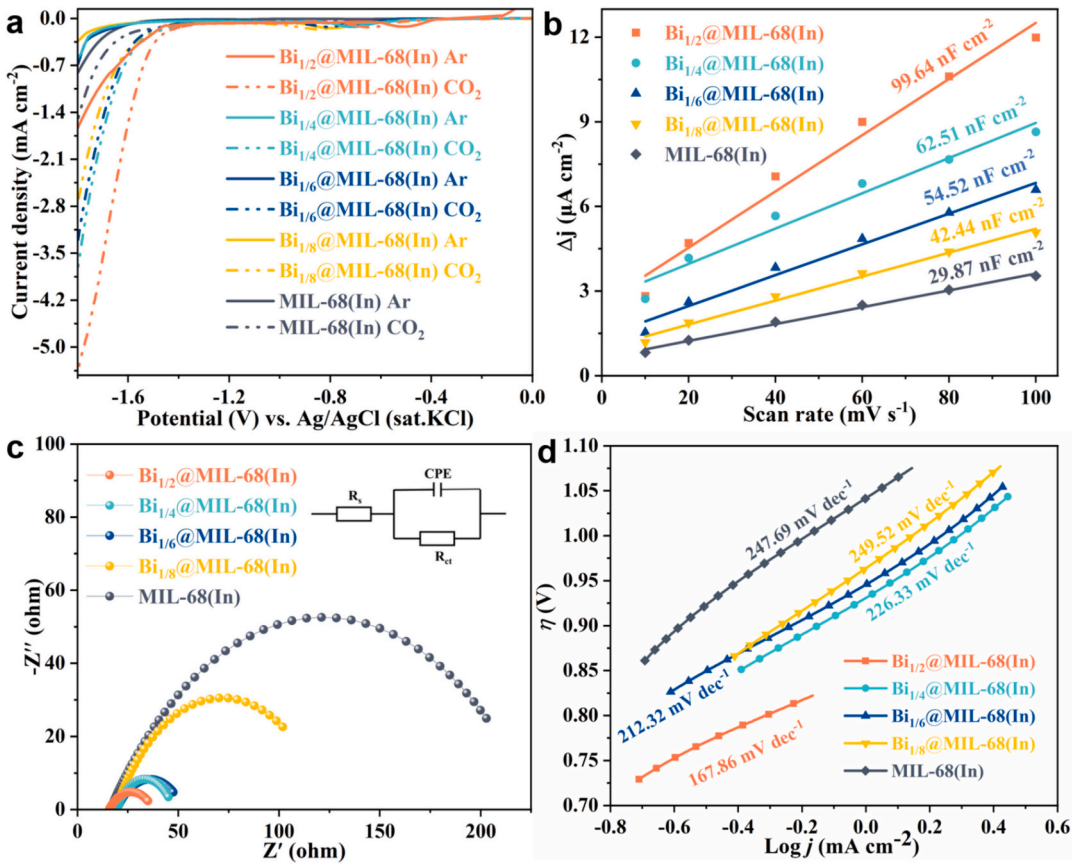

Fig. 4. Electrochemical characterization of MIL-68(In) and Bi$_x$@MIL-68(In) as ECO$_2$RR catalysts in 0.1 M KHCO$_3$ aqueous solution. (a) LSV curves under Ar-saturated (solid line) and CO$_2$-saturated (dashed line) conditions on glassy carbon electrodes; (b) ECSA comparison, (c) EIS plots, and (d) Tafel plots of MIL-68(In) and Bi$_x$@MIL-68(In).

this parameter is directly positively correlated with the double-layer capacitance (C_{dl}) of a catalyst [40,41]. The C_{dl} value of the material can be determined by analyzing the CV curves obtained at various sweep rates (**Fig. S7**). As illustrated in Fig. 4b, Bi$_{1/2}$@MIL-68(In) displayed a significantly higher C_{dl} compared with pure MIL-68(In), showing that Bi doping increased the number of active sites in MIL-68(In). Practically, this implies a denser distribution of active sites per unit area that could participate in the reaction, thereby markedly enhancing the catalytic performance in ECO$_2$RR.

To further investigate the kinetic mechanisms underlying the performance enhancement resulting from Bi doping, impedance assays were performed on all samples. In Fig. 4c, the impedance semicircle of pure MIL-68(In) was the most prominent, indicating that electron transfer was hindered and that limited electrocatalytic reactions occurred exclusively on MIL-68(In). In contrast, the fitted Nyquist plots of Bi$_{1/2}$@MIL-68(In) exhibited a comparatively smaller impedance radius, indicating a lower charge transfer resistance (R_{ct} = 22.13 Ω) and solution resistance (R_s = 15.65 Ω) during CO$_2$ reduction. The Bi$_{1/2}$@MIL-68(In) catalyst displayed a lower resistance to electron migration and facilitated a more efficient interfacial electron transfer mechanism. The actual values of all the R_s and R_{ct} are listed in **Table S1**. Bi-loaded Bi$_x$@MIL-68(In) also possessed rapid electron transfer kinetics. Lower electron transfer resistance in the catalyst enabled faster electron transport from the interior of the material to its surface during ECO$_2$RR. This enhanced electron mobility facilitated the adsorption of CO$_2$ on the catalyst surface, thereby promoting the generation of *COOH intermediates, which accelerated the formation of HCOOH during CO$_2$ reduction [42].

The Tafel slope serves as an indicator of the kinetics underlying the formation of HCOOH and can be used to elucidate a reaction mechanism. As demonstrated in Fig. 4d, Bi$_{1/2}$@MIL-68(In) exhibited the smallest Tafel slope (167.86 mV dec^{-1}), suggesting that its reaction kinetics for electrocatalytic reduction of CO$_2$ were the most rapid. In contrast to the Tafel slope of MIL-68(In) (247.69 mV dec^{-1}), Bi$_{1/2}$@MIL-68(In) exhibited a significantly higher electron transfer efficiency, in agreement with the EIS results.

The previous series of experiments demonstrated that Bi$_x$@MIL-68(In) was capable of electrocatalytically reducing CO$_2$ with a glassy carbon electrode. However, to enhance the practical industrial applications of this catalyst, a 1 × 2 cm^2 glass plate electrode was adopted for subsequent electrochemical investigations. Fig. 5a demonstrated that when deposited onto the glass plate electrode, the catalyst maintained significant electrocatalytic activity for CO$_2$ reduction. To investigate the product selectivity at different potentials, the products were analyzed using GC and IC (**Fig.S8-S10**). Fig. 5b illustrates that the FE for formic acid on Bi$_{1/2}$@MIL-68(In) catalyst initially increased and subsequently decreased upon decreasing the potential. A maximum value of 96.9 % was achieved at a potential of −1.7 V (vs. Ag/AgCl). At this same potential, gas products such as CO, H$_2$, C$_2$H$_4$, and C$_2$H$_6$ were detected by gas chromatography with a sum of their FE of 3 %. In the potential range of −1.5 to −1.8 V, the FE for formic acid on MIL-68(In) was lower than that of Bi$_{1/2}$@MIL-68(In). The FE_{HCOOH} of Bi$_{1/4}$@MIL68(In), Bi$_{1/6}$@MIL68(In), and Bi$_{1/8}$@MIL68(In) was further tested at −1.7 V, but none exceeded 75 % (**Fig. S11**), further demonstrating the higher formic acid selectivity of Bi$_{1/2}$@MIL68(In). The high activity and selectivity on Bi$_{1/2}$@MIL-68(In) for formic acid were attributed to the uniform attachment of small-sized bismuth oxide filaments onto the In-MOFs substrate. This configuration completely exposed the active sites, thereby enhancing the catalytic performance.

As depicted in Fig. 5c, the time-space yields on both Bi$_{1/2}$@MIL-68

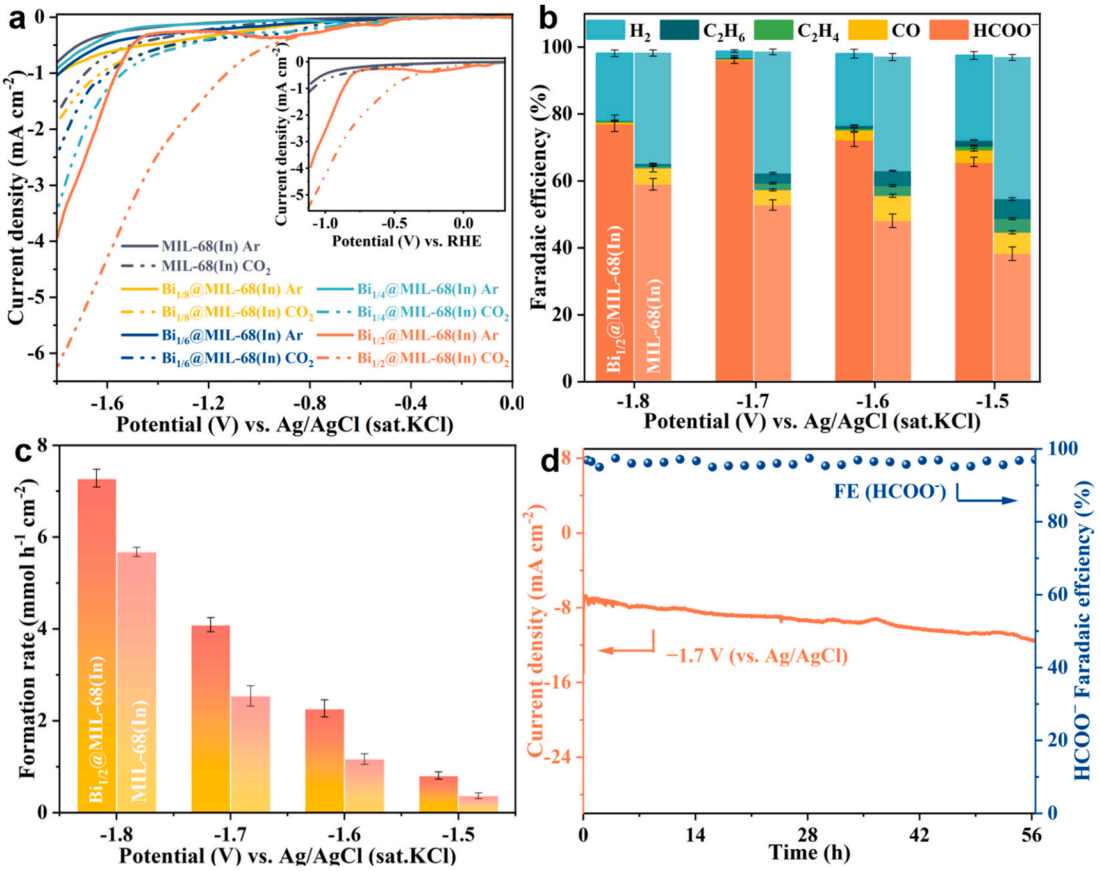

Fig. 5. (a) LSV curves of MIL-68(In) and Bi_x@MIL-68(In) on glass plates; (b) FE, and (c) time-space yields on MIL-68(In) and $Bi_{1/2}$@MIL-68(In); (d) The chronoamperometry response and time-dependent FE_{HCOO^-} of $Bi_{1/2}$@MIL-68(In) at −1.7 V (vs. Ag/AgCl). (Error bars for all data points are based on the standard deviation of 3 replicate experiments).

(In) and MIL-68(In) increased as the potential decreased, with $Bi_{1/2}$@MIL-68(In) exhibiting a higher formation rate. Fig. 5d shows that $Bi_{1/2}$@MIL-68(In) operated stably at −1.7 V for 56 h, demonstrating its excellent stability. The FE_{HCOOH} exceeded 95 % over the entire 56 h. The Faradaic efficiency and stability of $Bi_{1/2}$@MIL-68(In) were superior to those of other In-based or Bi-based catalysts [43–46] documented in the literature (**Table S2**).

3.3. *Theoretical insights into the catalytic mechanism*

The ECO_2RR mechanism on MIL-68(In) and $Bi_{1/2}$@MIL-68(In) catalysts was investigated by theoretical calculations. Fig. 6a illustrates the optimized geometry of MIL-68(In), as well as the structure resulting from the substitution of some In atoms with Bi atoms in MIL-68(In). The Gibbs free energy diagrams for the formation of HCOOH on MIL-68(In) and $Bi_{1/2}$@MIL-68(In) for ECO_2RR were calculated and shown in Fig. 6b. The corresponding energy barriers are shown in Fig. 6c. Specifically, the downslope energy barrier for CO_2 reduction in the first step from CO_2 to $*CO_2$ was −0.45 eV on MIL-68(In) and − 0.3 eV on $Bi_{1/2}$@MIL-68(In), demonstrating that CO_2 was more prone to activation on MIL-68(In). However, $Bi_{1/2}$@MIL-68(In) exhibited a relatively low energy barrier for the formation of *HCOOH (ΔG = 2.84 eV), which was lower than that of MIL-68(In) (ΔG = 3.13 eV), which resulted in a higher electrocatalytic activity for ECO_2RR towards HCOOH on $Bi_{1/2}$@MIL-68(In). Compared with MIL-68(In), $Bi_{1/2}$@MIL-68(In) significantly reduced the free energy of generation by stabilizing the HCOO* intermediate, which greatly facilitated the reduction of CO_2 to HCOOH.

4. Conclusions

In this study, a series of Bi_2O_3–loaded indium–organic framework catalysts (Bi_x@MIL-68(In)) with different Bi^{3+} doping ratios (x = 1/2, 1/4, 1/6, 1/8) were synthesized via a simple hydrothermal method. Notably, $Bi_{1/2}$@MIL-68(In) exhibited higher electrocatalytic performance for CO_2 reduction than MIL-68(In). In an H-type electrolytic cell, this catalyst achieved a Faradaic efficiency of 96.9 % for formic acid production at −1.7 V (vs. Ag/AgCl).

The experimental findings revealed that Bi^{3+} doping significantly improved the electrical conductivity of the catalyst and accelerated electron transfer, thereby enhancing its overall performance. Moreover, Bi_2O_3 incorporation into the MIL-68(In) framework increased the number of active sites on the catalyst surface, which promoted CO_2 adsorption and activation, leading to increased formic acid yield. Theoretical calculations further elucidated the catalytic mechanism. $Bi_{1/2}$@MIL-68(In) stabilized the HCOO* intermediate, reduced the free energy barrier for HCOOH formation, and enhanced the electrocatalytic activity towards CO_2 reduction.

This study highlights the potential of metal–organic frameworks (MOFs) as structural scaffolds for incorporating secondary metals to enhance catalytic performance. These findings provide valuable guidance for developing MOF-supported metal electrocatalysts and highly efficient CO_2 reduction catalysts.

CRediT authorship contribution statement

Fajun Li: Writing – review & editing, Project administration. **Yuqi Ma:** Formal analysis, Data curation. **Lei Zhao:** Investigation. **Lu Han:** Methodology. **Xuancheng Gong:** Software. **Yulu Zhang:** Formal

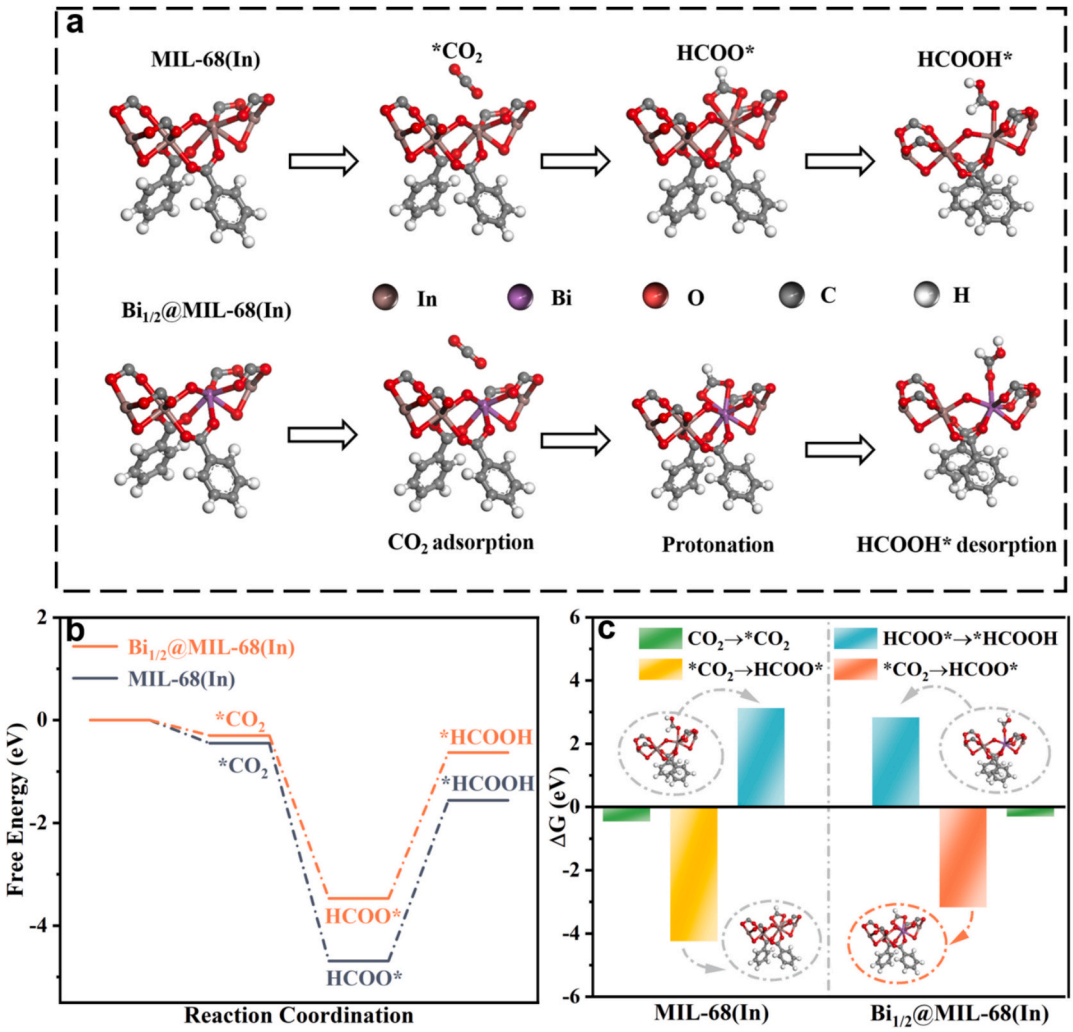

Fig. 6. Theoretical calculations: (a) Schematic representation of the mechanism for formic acid formation on MIL-68(In) and $Bi_{1/2}$@MIL-68(In); (b) Calculated Gibbs free energy diagrams for ECO_2RR to HCOOH on MIL-68(In) and $Bi_{1/2}$@MIL-68(In); (c) Calculated ΔG for HCOOH production over MIL-68(In) and $Bi_{1/2}$@MIL-68 (In) sites.

analysis. **Pengfei Lu:** Software, Conceptualization. **Guizhi Wang:** Formal analysis. **Zhisheng Shi:** Project administration, Methodology. **Zhong Jin:** Project administration, Investigation.

Declaration of competing interest

The authors declare that they have no known competing financial interests or personal relationships that could have influenced the work reported in this paper.

Acknowledgments

This work was supported by Anhui Province Young Backbone Teachers' In-country Study Visit Programme (JNFX2023067), Reserve Candidates for Academic and Technical Leaders (2024XJHB07), Scientific Research Platform (2023KYPT03, 2021XJPT07), and Jointly Cultivated Postgraduate Scientific Research Innovation Fund Project (2025KYCX13). This work was also supported by the National Natural Science Foundation of China (22206145), the Project of Anhui Province (2023AH030100, 2024AH051822), Scientific research project of Suzhou University (2024yzd12, 2021BSK053), and the Anhui Postdoctoral Scientific Research Program Foundation (No. 2024B805), the Innovation and Entrepreneurship Training Program for College Students (202410363058).

Appendix A. Supplementary data

Supplementary data to this article can be found online at https://doi.org/10.1016/j.jcis.2025.138251.

Data availability

The data that has been used is confidential.

References

[1] X. Chen, L. Cavallo, K.-W. Huang, Selectivity of electrochemical CO_2 reduction on metal electrodes: the role of the surface oxidized layer, ACS Catal. 13 (19) (2023) 13089–13100.
[2] W. Zhang, C. Zhao, Y. Yang, R. Chen, Y. Wu, J. Dai, Y. Zhang, H. Liu, M. Liu, Highly dispersed atomic-level Ni active sites confined in defects for efficient electrocatalytic reduction of carbon dioxide, J. Energy Chem. 99 (2024) 1–10.
[3] A. Fortunato, H. Herwartz, R.E. López, B. Figueroa, E., Carbon dioxide atmospheric concentration and hydrometeorological disasters, Nat. Hazards 112 (1) (2022) 57–74.
[4] S.S.A. Shah, M. Sufyan Javed, T. Najam, C. Molochas, N.A. Khan, M.A. Nazir, M. Xu, P. Tsiakaras, S.-J. Bao, Metal oxides for the electrocatalytic reduction of carbon dioxide: mechanism of active sites, composites, interface and defect engineering strategies, Coord. Chem. Rev. 471 (2022) 214716.
[5] G. Wen, B. Ren, X. Wang, D. Luo, H. Dou, Y. Zheng, R. Gao, J. Gostick, A. Yu, Z. Chen, Continuous CO_2 electrolysis using a CO_2 exsolution-induced flow cell, Nat. Energy 7 (10) (2022) 978–988.

[6] B. Ren, G. Wen, R. Gao, D. Luo, Z. Zhang, W. Qiu, Q. Ma, X. Wang, Y. Cui, L. Ricardez-Sandoval, et al., Nano-crumples induced Sn-Bi bimetallic interface pattern with moderate electron bank for highly efficient CO_2 electroreduction, Nat. Commun. 13 (1) (2022) 2486.

[7] X. Zhang, B. Ren, H. Li, S. Liu, H. Xiong, S. Dong, Y. Li, D. Luo, Y. Cui, G. Wen, et al., Regulating ethane and ethylene synthesis by proton corridor microenvironment for CO_2 electrolysis, J. Energy Chem. 87 (2023) 368–377.

[8] C. Liu, R.-T. Guo, H.-W. Zhu, H.-F. Cui, M.-Y. Liu, W.-G. Pan, Cu_2O-based catalysts applied for electrocatalytic CO_2 reduction: a review, J. Mater. Chem. A 12 (2024) 31769–31796.

[9] K. Fernández-Caso, M. Molera, T. Andreu, J. Solla-Gullón, V. Montiel, G. Díaz-Sainz, M. Álvarez-Guerra, A. Irabien, Coupling glycerol oxidation reaction using Ni-CO foam anodes to CO_2 electroreduction in gas-phase for continuous co-valorization, Chem. Eng. J. 480 (2024) 147908.

[10] W. Ye, X. Guo, T. Ma, A review on electrochemical synthesized copper-based catalysts for electrochemical reduction of CO_2 to C_{2+} products, Chem. Eng. J. 414 (2021) 128825.

[11] H. Shen, T. Peppel, J. Strunk, Z. Sun, Photocatalytic reduction of CO_2 by metal-free-based materials: recent advances and future perspective, Solar RRL: Rapid Res. Lett. 4 (8) (2020) 1900546.

[12] S. Chatterjee, I. Dutta, Y. Lum, Z.P. Lai, K.W. Huang, Enabling storage and utilization of low-carbon electricity: power to formic acid, Energy Environ. Sci. 14 (3) (2021) 1194–1246.

[13] N. Han, P. Ding, L. He, Y. Li, Y. Li, Promises of main group metal–based nanostructured materials for electrochemical CO_2 reduction to formate, Adv. Energy Mater. 10 (11) (2020) 1902338.

[14] L. Jia, M.Z. Sun, J. Xu, X. Zhao, R. Zhou, B.B. Pan, L. Wang, N. Han, B.L. Huang, Y. G. Li, Phase-dependent electrocatalytic CO_2 reduction on Pd_3Bi nanocrystals, Angew. Chem. Int. Ed. 60 (40) (2021) 21741–21745.

[15] M. Grasemann, G. Laurenczy, Formic acid as a hydrogen source-recent developments and future trends, Energy Environ. Sci. 5 (8) (2012) 8171–8181.

[16] H. Yang, N. Han, J. Deng, J. Wu, Y. Wang, Y. Hu, P. Ding, Y. Li, Y. Li, J. Lu, Selective CO_2 reduction on 2D mesoporous Bi nanosheets, Adv. Energy Mater. 8 (35) (2018) 1801536.

[17] C.S. Cao, D.D. Ma, J.F. Gu, X.Y. Xie, G. Zeng, X.F. Li, S.G. Han, Q.L. Zhu, X.T. Wu, Q. Xu, Metal-organic layers leading to atomically thin Bismuthene for efficient carbon dioxide electroreduction to liquid fuel, Angew. Chem. Int. Ed. 59 (35) (2020) 15014–15020.

[18] H. Shang, T. Wang, J. Pei, Z. Jiang, D. Zhou, Y. Wang, H. Li, J. Dong, Z. Zhuang, W. Chen, et al., Design of a single-atom Indiumδ^+–N_4 interface for efficient electroreduction of CO_2 to formate, Angew. Chem. Int. Ed. 59 (50) (2020) 22465–22469.

[19] W. Luo, W. Xie, M. Li, J. Zhang, A. Züttel, 3D hierarchical porous indium catalyst for highly efficient electroreduction of CO_2, J. Mater. Chem. A 7 (9) (2019) 4505–4515.

[20] S.H. Li, S. Hu, H. Liu, J. Liu, X. Kang, S. Ge, Z. Zhang, Q. Yu, B. Liu, Two-dimensional metal coordination polymer derived indium nanosheet for efficient carbon dioxide reduction to Formate, ACS Nano 17 (10) (2023) 9338–9346.

[21] B. Wulan, X. Cao, D. Tan, J. Ma, J. Zhang, To stabilize oxygen on in/In_2O_3 heterostructure via joule heating for efficient electrocatalytic CO_2 reduction, Adv. Funct. Mater. 33 (1) (2023) 2209114.

[22] Q. Cheng, M. Huang, L. Xiao, S. Mou, X. Zhao, Y. Xie, G. Jiang, X. Jiang, F. Dong, Unraveling the influence of oxygen vacancy concentration on Electrocatalytic CO_2 reduction to Formate over indium oxide catalysts, ACS Catal. 13 (6) (2023) 4021–4029.

[23] Z. Liang, C. Qu, W. Guo, R. Zou, Q. Xu, Pristine metal–organic frameworks and their composites for energy storage and conversion, Adv. Mater. 30 (37) (2018) 1702891.

[24] W. Xia, A. Mahmood, R. Zou, Q. Xu, Metal–organic frameworks and their derived nanostructures for electrochemical energy storage and conversion, Energy Environ. Sci. 8 (7) (2015) 1837–1866.

[25] L.-X. Liu, C. Qin, T. Deng, L. Sun, Z. Chen, X. Han, Cu MOF-based electrocatalysts for CO_2 reduction to multi-carbon products, J. Mater. Chem. A 12 (39) (2024) 26421–26438.

[26] F. Yang, D. Zhu, C. Xia, Z. Shahid, S. Chen, B.Y. Xia, Copper-organic frameworks for electrocatalytic carbon dioxide reduction, Coord. Chem. Rev. 517 (2024) 216021.

[27] Y.-T. Zheng, S. Li, N.-Y. Huang, X. Li, Q. Xu, Recent advances in metal–organic framework-derived materials for electrocatalytic and photocatalytic CO_2 reduction, Coord. Chem. Rev. 510 (2024) 215858.

[28] B. Hedau, S.-J. Park, B.-C. Kang, T.-J. Ha, Bifunctional carbon quantum dot-embedded metal-organic framework nanohybrid as a highly efficient electrocatalyst for water splitting and CO_2 reduction, Carbon 216 (2024) 118527.

[29] D.-H. Nam, O. Shekhah, G. Lee, A. Mallick, H. Jiang, F. Li, B. Chen, J. Wicks, M. Eddaoudi, E.H. Sargent, Intermediate binding control using metal–organic frameworks enhances electrochemical CO_2 reduction, J. Am. Chem. Soc. 142 (51) (2020) 21513–21521.

[30] Z. Wang, Y. Zhou, C. Xia, W. Guo, B. You, B.Y. Xia, Efficient Electroconversion of carbon dioxide to Formate by a reconstructed amino-functionalized indium-organic framework electrocatalyst, Angew. Chem. Int. Ed. 60 (35) (2021) 19107–19112.

[31] J. Yuan, M. Pudukudy, T. Hu, Y. Liu, X. Luo, Y. Zhi, H. Su, L. Jiang, S. Shan, CeO_x-coupled MIL-125-derived C-TiO_2 catalysts for the enhanced photocatalytic abatement of tetracycline under visible light irradiation, Appl. Surf. Sci. 557 (2021) 149829.

[32] B. Pan, G. Yuan, X. Zhao, N. Han, Y. Huang, K. Feng, C. Cheng, J. Zhong, L. Zhang, Y. Wang, et al., Highly dispersed indium oxide nanoparticles supported on carbon nanorods enabling efficient electrochemical CO_2 reduction, Small Sci. 1 (10) (2021) 2100029.

[33] Z. Wang, Y. Zhou, D. Liu, R. Qi, C. Xia, M. Li, B. You, B.Y. Xia, Carbon-confined indium oxides for efficient carbon dioxide reduction in a solid-state electrolyte flow cell, Angew. Chem. Int. Ed. 61 (21) (2022) e202200552.

[34] C. Volkringer, M. Meddouri, T. Loiseau, N. Guillou, J. Marrot, G. Férey, M. Haouas, F. Taulelle, N. Audebrand, M. Latroche, The Kagomé topology of the gallium and indium metal-organic framework types with a MIL-68 structure: synthesis, XRD, solid-state NMR characterizations, and hydrogen adsorption, Inorg. Chem. 47 (24) (2008) 11892–11901.

[35] L. Wu, M. Xue, S.-L. Qiu, G. Chaplais, A. Simon-Masseron, J. Patarin, Amino-modified MIL-68(In) with enhanced hydrogen and carbon dioxide sorption enthalpy, Microporous Mesoporous Mater. 157 (2012) 75–81.

[36] H. Tan, Z. Zhao, W.-B. Zhu, E.N. Coker, B. Li, M. Zheng, W. Yu, H. Fan, Z. Sun, Oxygen vacancy enhanced photocatalytic activity of Pervoskite $SrTiO_3$, ACS Appl. Mater. Interfaces 6 (21) (2014) 19184–19190.

[37] X. Cao, B. Wulan, Y. Wang, J. Ma, S. Hou, J. Zhang, Atomic bismuth induced ensemble sites with indium towards highly efficient and stable electrocatalytic reduction of carbon dioxide, Sci. Bull. 68 (10) (2023) 1008–1016.

[38] Y. Gao, H. Xiao, X. Ma, Z. Yue, C. Liu, M. Zhao, L. Zhang, J. Zhang, E. Luo, T. Hu, et al., Gallium–indium bimetal sites in the indium–gallium metal organic framework for efficient electrocatalytic reduction of carbon dioxide into formate, J. Mater. Chem. A 12 (14) (2024) 8272–8280.

[39] R. Liang, R. Huang, X. Wang, S. Ying, G. Yan, L. Wu, Functionalized MIL-68(In) for the photocatalytic treatment of Cr(VI)-containing simulation wastewater: electronic effects of ligand substitution, Appl. Surf. Sci. 464 (2019) 396–403.

[40] F. Yang, A.O. Elnabawy, R. Schimmenti, P. Song, J. Wang, Z. Peng, S. Yao, R. Deng, S. Song, Y. Lin, et al., Bismuthene for highly efficient carbon dioxide electroreduction reaction, Nat. Commun. 11 (1) (2020) 1088.

[41] G. Jia, Y. Wang, M. Sun, H. Zhang, L. Li, Y. Shi, L. Zhang, X. Cui, T.W.B. Lo, B. Huang, et al., Size effects of highly dispersed bismuth nanoparticles on electrocatalytic reduction of carbon dioxide to formic acid, J. Am. Chem. Soc. 145 (25) (2023) 14133–14142.

[42] X. Du, P. Zhang, G. Zhang, H. Gao, L. Zhang, M. Zhang, T. Wang, J. Gong, Confinement of ionomer for electrocatalytic CO_2 reduction reaction via efficient mass transfer pathways, Natl. Sci. Rev. 11 (2) (2024) nwad149.

[43] S.-Z. Hou, X.-D. Zhang, W.-W. Yuan, Y.-X. Li, Z.-Y. Gu, Indium-based metal–organic framework for high-performance electroreduction of CO_2 to formate, Inorg. Chem. 59 (16) (2020) 11298–11304.

[44] W. Yang, Y. Zhao, S. Chen, W. Ren, X. Chen, C. Jia, Z. Su, Y. Wang, C. Zhao, Defective indium/indium oxide heterostructures for highly selective carbon dioxide electrocatalysis, Inorg. Chem. 59 (17) (2020) 12437–12444.

[45] L. Wang, P. Liu, Y. Xu, Y. Zhao, N. Xue, X. Guo, L. Peng, Y. Zhu, M. Ding, Q. Wang, et al., Enhanced catalytic activity and stability of bismuth nanosheets decorated by 3-aminopropyltriethoxysilane for efficient electrochemical reduction of CO_2, Appl. Catal. B Environ. 298 (2021) 120602.

[46] D. Tan, W. Lee, Y.E. Kim, Y.N. Ko, M.H. Youn, Y.E. Jeon, J. Hong, J.E. Park, J. Seo, S.K. Jeong, et al., In–Bi Electrocatalyst for the reduction of CO_2 to Formate in a wide potential window, ACS Appl. Mater. Interfaces 14 (25) (2022) 28890–28899.